Third International Conference on Inverse Design Concepts and Optimization in Engineering Sciences
(ICIDES-III). Editor: G.S. Dulikravich, Washington D.C., October 23-25, 1991.

N92-13956

# RESEARCH ON INVERSE METHODS AND OPTIMIZATION IN ITALY

Francesco Larocca
FIAT AVIO, Corso Ferrucci 112, 10129, Turin Italy

p. 20

## 1 Introduction

The paper deals with the research activities in Italy on inverse design and optimization. The review is focused on aerodynamic aspects in turbomachinery and wing sections design.

Inverse design of blade rows and ducts of turbomachinery in subsonic and transonic regime are illustrated here by the contributions of "Politecnico di Torino" and turbomachinery industry (FIAT AVIO).
As far as turbomachinery design is concerned, the development of an optimization technique is shown by the contributions of the "Universita' di Genova".

Contributions from the " Universita' di Bari " illustrate recent progress in aerfoils design in the field of subsonic flow.

## 2 Turbomachinery Components

### 2.1 Design of cascade and ducts in transonic flow

A methodology to solve inverse design problems for channels and blade rows, assuming the flow to be multidimensional and the fluid inviscid, compressible and ideal, is described in [1]. The methodology is based on the procedures described in [2] for the solution of inverse problems in 2D channels, in [3] for 2D inverse cascade problems, in [5] for 3D inverse blade rows problems. An updated version of the methodology is described in [6] for both 2D and 3D inverse problems in channels and blade rows.
The basic idea is described in [2]. Briefly, a time-dependent computation is performed in a duct, where a distribution of pressure is prescribed on a wall, the geometry of which is unknown and has to be determined. Such a wall is a boundary of the flow field and it is assumed as a flexible and impermeable surface. Some initial configuration is guessed for the shape of the wall and for the internal flowfield. During the following transient the flexible wall move in a wavy fashion and, at the end, it will assume the steady shape required by the prescribed pressure on it and in agreement with the steady internal flow.
A coordinate transformation is used in order to map the physical region, whose shape depends on time, into a computational domain, whose shape is independent of time. The Euler equations are integrated in time by a finite difference method on the time-dependent, body fitted, grid defined by the mapping.
In order to show the way the solution is gained in time, we report here one of the examples of [2]. The Ringleb flow [8] was taken as benchmark case. A set of streamlines $\psi = const$ of the Ringleb flow are plotted in fig. 1. Once two streamlines are selected, they may be regarded as the solid walls of a channel, and, from the point of view of an inverse problem, the theoretical pressure acting on these may be taken as the design input datum. The chosen channel is in the transonic region, and is confined by the streamlines $\psi = 0.8$, $\psi = 1.0$ and by the radial coordinate lines $\theta = 40^o$, $\theta = 90^o$.
Fig. 2 shows the shapes of the walls during the transient (solid lines), from the initial guessed configuration ($K = 0$) to the final one ($K = 500$). The dots denote the theoretical location of the streamlines. The maximum relative error of the location of the wall points is less than 0.6%, while the maximum relative error of the computed Mach number in the whole flow field is less than 0.4%

Since [2] was published, several improvements have been done. Upwind numerical schemes have been adopted to attain consistency with the wave propagation phenomena described by the Euler equations, as a consequence the computation at the boundaries has been improved; the extension to 3D problems has been shown feasible; different formulations have been attempted. The path of the evolution runs from [2] to [6].

### 2.1.1 The cascade problem

For a 2D cascade of airfoils, the inverse problem consists of finding the geometry of a cascade producing a flow of which some parameters are prescribed. There is a certain freedom in the formulation of the problem. We confine the discussion in the present report to problem for the 2D and 3D cases, where, in addition to suitable condition at infinity one may prescribe the distribution of thickness and load along the chord of a profile, and inquire for the geometry of the camber line.
In [2] - [6], the problems are solved by using the technique briefly outlined in the previous section: a time-dependent computation is performed, in which the boundary conditions are imposed according to the formulation of the inverse problem, until a steady state is reached asymptotically. The contours of the blades are considered as impermeable but perfectly deformable. An initial geometry is assumed. Since such a geometry is incompatible with a steady motion, consistent with the prescribed conditions, a transient is generated. During the transient, the walls of the blades change in shape, in order to satisfy the condition of impenetrability. The solution of the inverse problem is given by a geometry obtained asymptotically.
The reader may refer to Ref.[3] and Ref.[7] for the discussion of the 2D different problem formulations.

We proceed now to describe the process, in particular the boundary conditions, that have been chosen to generate the solution, confining ourself to the physical viewpoint.
Figs. 3a) and 3b) show typical initial and final configurations. The flow is assumed to be confined between two consecutive blades, the arcs BC, and two parallel lines issuing from the leading edge and the trealing edge of the blades. The lines in front of the blades are denoted by AB. The lines behind the blades are denoted by CD. Such boundaries are assumed to be impermeable and perfectly deformable; therefore, we can think in terms of a flow within a channel, the geometry of which may change in time, although its width (measured parallel to the $y$-axis) is independent of time. The channel is confined by the permeable boundaries AA and DD, upstream and downstream, respectively. The inlet boundary AA is considered fixed in time, whereas the exit boundary DD can slide upwards and downwards, maintaining a constant pitch. A time-dependent computational grid, which fits the boundaries, is defined inside the channel.
The design data are prescribed, according to problem formulation, by giving the distribution of thickness $\tau(x)$ and pressure jump between the two sides of the blades, $\Delta p(x)$. Since the flow is periodic, the upper and lower boundaries of figs. 3 can be reduced to a single boundary for a single blade, as in fig. 4. Note that the upper part of the ABCD line in figs.3 is the lower boundary in fig.4, and viceversa.
The arcs, AB and CD are deformable and impermeable interfaces, across which the pressure is continuous but the tangential velocity component may be discontinuous. In formulating the boundary conditions, the whole ABCD arc can be treated homogeneously. The interfaces can be considered as surfaces of blades for which a vanishing thickness and a vanishing pressure jump are prescribed. With this convention in mind, we procede to describe the technique for any blade surface.
In fig. 5 we show two grid points on two different sides of the blade, at the same abscissa. The velocity vector is decomposed along the tangent and the normal to the blade at each point. Since the blade is impermeable, the two flow velocities and the blade velocity must have the same normal component. Moreover, by imposing the pressure jump $\Delta p(x)$ to be constant in time, the boundary conditions that allow the geometry and the the flow to be updated at each computational step, are obtained.
At the inlet boundary AA (figs.3) we prescribe the total pressure, the total temperature and the flow angle, if the flow is subsonic, whereas all the flow quantities are prescribed if the flow is axially supersonic.
At the exit boundary DD no boundary conditions are needed if the flow is axially supersonic, while in the case of subsonic flow, the kind of boundary conditions to be enforced has to be selected carefully, in fact, as it is discussed in [1] and [3], the inverse problem has not an uniquely defined solution. The kind of boundary conditions that is used selects one solution among the possible ones.

The numerical process used approximates the governing equations written in quasi-linear form, as a consequence it is not conservative and weak solutions are not captured spontaneusly, but they need some special

treatment. This shortcoming is the price to be paid for the main advantage that our numerical process offers: the capability of computing the boundaries in a way consistent with domain of dependence due to the hyperbolic nature of the governing equations, avoiding the need for spurious additional numerical boundary conditions. This point is crucial for the success of method,in fact the computation in a domain whose physical shape depends on the solution is very sensitive to the way the boundary condition are enforced and any mistreatment may produce catastrophic instabilities.
Moreover, the inverse problems that generally one asks to be solved are shockless and the need for shock-capturing capability is rare; if this capability is requested, the scheme can be easily converted in a conservative Flux Vector Splitting scheme, as described in [12].

In the early formulation [3]-[5], a numerical procedure to solve inverse problems has been developed according to the *lambda*-scheme [9] and [10]. Briefly, the wave system affecting a given point in an unsteady flow field is described by four orthogonal waves. The $\lambda$-scheme uses one-sided differences to approximate the compatibility equations relative to the four waves, according to their direction of propagation and, as a consequence, satisfying the domain of dependence. The computations of a transonic shockless compression comes quite accurate and, besides that, the computation at the boundaries is simple and naturally suited for this kind of numerical scheme based on compatibility equations, avoiding almost completely the need for numerical additional boundary conditions.

Two numerical examples are here presented according to the selected formulation and prescribing the static pressure $p_e$ as exit boundary condition. Further examples are shown in Ref. [3].
Fig. 6 shows the initial configuration and fig. 7 the steady solution to the inverse problem for the case corresponding to

$$\tau = .025\,[1-\cos(2\pi x)] \qquad \Delta p = c\,[1-\cos(2\pi x)] \qquad (0 < x < 1)$$

The ratio $p_e/p^o$ between downstream pressure and total pressure is 0.8, the upstream flow angle $\sigma_i$ is $20^o$, and the upstream nondimensional total temperature $\Theta^o$ is 1, while $c = .1$. Both this case and the following one have been computed using 40 intervals in $x$ and 10 in $y$.
A check on the accuracy of the computation is shown in fig. 8, where the theoretical behavior of the y-momentum is compared with the numerical result. The maximum error is less then 1%.
The case of fig. 9 has the same $\tau$, $\sigma_i$, and $\Theta^o$ as in the preceding case, but $c = 0.15$ and $p_e/p^o = 0.71$.
The resulting cascade is supercritical but unchoked and shockless. It can be seen from the isoMach lines of fig. 9 that a supersonic bubble appears on the upper side of the blade, but the lower side is entirely subsonic. The pressure cannot be discontinuous on the subsonic side; therefore, it must be continuous on the supersonic side as well, since $\Delta p$ is prescribed as a continuous function of $x$.

A further example is presented in fig. 10. It refers to the axial cascade with supersonic inlet Mach number, but having subsonic axial component. In this case the regime of unique incidence is established and it requires a boundary condition at inlet wich does not violate the simple wave region upstream of the cascade. This is obtained by imposing, at the inlet boundary, besides the total pressure and total temperature, the compatibilty relationship between Mach number and flow direction along a Mach line for steady supersonic flow. In fig. 10 the isomach contours are presented; the inlet Mach number is equal to 1.19, while th exit flow is subsonic and the cascade is shockless. In fig. 11, as a check, in the odograph plane the upstream flow field is presented. The simple wave region is well described, as it can be seen by the points belonging to a unique epicycloid.

In Ref. [4] a different formulation of the 2-D inverse problem is attempted: instead of looking for the shape of the walls, which in turn define the grid, it is looked for a whole orthogonal grid which adapts itself to the solution of the inverse problem. the Euler equations are written by assuming a set of indipendent variable that, at the steady state, coincide with the stream function and with a curvilinear co-ordinate along the lines orthogonal to the streamlines. The Euler equation so written are integrated in time according to the $\lambda$-scheme, the numerical process turns out very simple and quite accurate. The main drawback of method presented in [4], is that such method has not a straighforward extension to 3-D problems.

The success of a computational method aiming to solve multidimensional problems governed by the time-dependent Euler equations lies mainly and obviously on the integration scheme and on the treatment of the boundaries. The $\lambda$-formulation shows good qualities in both respects, it does not violate the domains of dependence and it allows the boundaries to be treated in a way consistent with the wave phenomena approximated in the inner flow field. Nevertheless, the upwind schemes to approximate multidimensional wave phenomena have a sort of weakness being necessarily based on the approximation of waves propagating along a finite number of directions, while the possible directions along which actual waves propagate are infinite. The problem is addressed in Ref. [10], and, more recently, in Ref. [11]

Following Ref. [11], the 3D time-dependent Euler equations written in tensor notations, can be rearranged in a form suitable for upwind discretization by decomposing the 3D unsteady motion as due to waves fronts parallel to the coordinate surfaces; the resulting set of equations prompts an upwind discretization that preserves the 3D nature of the actual flow and that is particularly convenient from the point of view of the treatment of the boundaries.
The resulting scheme is very close to the $\lambda$-scheme, coinciding with it for orthogonal grids; moreover, the boundaries can be treated avoiding completely the need for local frames of references and additional boundary conditions, even in the case of non orthogonal grid. Details on this matter can be found in [11].

### 2.1.2 Examples

Here three numerical results are presented: the first one refers to the design of a 3D rotational, transonic, convergent-divergent nozzle, while the other two refer to the design of turbomachinery bladings. In order to test the capabilities of the present inverse technique, in Ref. [1] the authors choose an example with a distorted geometry, quite far from the guessed initial one. Fig. 12a) shows the 3D view of the initial configuration and Fig.12b) the final one that solves the inverse problem. The solid walls are planes. The design pressure distribution on the lower moveable wall is

$$p_d = .8 - .7x^3$$

on the upper wall:

$$p_e = .8 - .35[1 - \cos(\pi x^3)]$$

On the inlet boundary the total temperature is kept uniform and constant in time $\Theta^0 = 1$, the flow velocity has the direction of the $x^3$ coordinate lines and the total pressure obeys the law:

$$p^0 = 1 - \Delta p^0 (y^1 - y^1_c)/(y^1_b - y^1_c); \qquad \Delta p^0 = .1$$

The resulting flow is rotational and non homoentropic.
Figg.13a), 13b) show the isoMach lines over the left and right solid walls, Figg. 14a), 14b) over the upper and the lower moveable walls and Figg. 15a), 15b) over the inlet and exit surfaces, respectively. Figg. 16a), 16b) show the constant-entropy lines on the inlet and exit surfaces, respectively.
The second example refers to the design of the blades of a stator. Figg. 17a), 17b), show the initial and final 3D view, respectively. The tip and hub solid annulus walls are cylindrical with $r_t/r_h = 1.5$.
The design thickness and the design loading are, respectively:

$$\tau = .07 \sin\left[\pi \frac{y^3 - y^3_l}{y^3_t - y^3_l}\right] \qquad \Delta p = .08 \sin\left[\pi \frac{y^3 - y^3_l}{y^3_t - y^3_l}\right]$$

with $y^3_t - y^3_l$ =axial chord.
At the inlet boundary the flow is axial. The total temperature is kept constant $\Theta^0 = 1$, while the tototal pressure is distorted:

$$p^0 = g\sqrt{y^1} + h$$

with $g = .1/(\sqrt{r_t} - \sqrt{r_h})$, $h = 1. - g\sqrt{r_t}$.
At the exit surface, a distribution of pressure, in agreement with an approximate solution based on the radial equilibrium theory, is given as boundary condition, with $p_h = .7$ at hub radius.
Figg. 18a), 18b) show the isoMach lines on the blade to blade surfaces at the hub and tip radii, Figg. 19a), 19b) on the pressure and suction sides of the blades, respectively. Figg. 20a) and 20b) show the constant entropy lines at the inlet and exit surfaces.

The constant entropy surfaces coincide with stream-surfaces; as it has been pointed out in Ref. [5], looking at Figg. 20a) and 20b) one would expect to see the typical rotation of such surfaces as consequence of the secondary flows generated in 3D rotational flow. Actually, a streamwise component of the vorticity is correctly generated, it does not reveal itself as a rotation of the streamtubes, but rather as a peculiar twisting of the blades: the loading is prescribed as design datum and it cannot be decreased as a consequence of secondary flows, but the lower is the total pressure (and density) the higher the deflection to provide such loading.
Finally, two integral checks have been done on the continuity and angular momentum of the computed flow field: Fig. 21 shows the mass flow computed on cross sections along the blade to blade channel; Fig. 22 compares the angular momentum evaluated on cross sections along the channel with the corrisponding theoretical torque due to the design loading.
In the third example the annulus walls form a conical surface at hub radius, and a cylindrical surface at tip radius. The flow at entry is assumed to have axial direction, with constant total temperature and a parabolic distribution of total pressure, the smallest being at hub radius. A certain distribution of thickness and pressure jump as functions of the radial and axial coordinates are assumed, $\tau = g(y^1, y^3)$, $\Delta p = f(y^1, y^3)$. At the exit surface, a distribution of pressure, in agreement with an approximate solution based on the radial equilibrium theory, is given as boundary condition, as well as in the previous example.
The initial configuration of the blade row is shown in fig. 23a). The blades are without camber and twist. Fig. 23b) shows the final configuration of the blade row. Figg. 24 and 25 represent the isoMach lines of the initial and final configuration of blade to blade section at hub radius, respectively. Figg. 26-28 represent the final configurations of the intermediate and tip blade to blade sections. The threedimensional nature of the flow field and the twisting of blades is shown in these results.
The flow is transonic, in fact a supersonic bubble extends from hub to tip on the section side. Figg. 29 and 30 show the isoMach lines on the projection on the meridional plane of the suction and pressure sides of the blades, respectively. Finally, figg. 31a) and 31b) show constant entropy lines on the sections normal to the axis, corresponding to the trailing edges and the exit of the streamtube.
The constant entropy surfaces coincide with stream-surfaces. Figg. 31a) and 31b) show the absence of the typical rotation of such surfaces and the peculiar twisting of the blade to blade channel, as well as in the previous example.

## 2.2 Design optimization of axial compressor

The aerothermodynamic design of turbomachines requires a number of indipendent parameters which results in a multiplicity of possible design configurations.
In order to have an optimized design of turbomachinery components, the choice of many design parameters requires an optimization problem to be solved in an early stage in the design cycle. The objective function in a general optimization problem represents a basis for the choice between various equally acceptable designs.

A computational procedure for design and optimization of axial turbomachines has been presented in [15]. The geometrical and fluid dynamic optimized quantities are obtained by coupling non linear minimization algorithms with methods for flow analysis and design. In the early formulation [16], the optimized design methodology uses the fluid dynamic analysis at mean diameter for axial turbine/compressors stages.
The optimization procedure presented in [15] and [16], is based on a constrained non linear minimization problem and is obtained by using three different methods: *Monte Carlo*, *Simplex* and *Gradient*. The numerical optimization strategies used in [16], based on a combination of the previous methods, has shown that the best results are obtained in general by enforcing the three methods sequentially.

In the work presented in [17], the authors used objective functions that are composed not only of a single variable, but of a combination of variables. This is done in order to avoid the improvement of a single quantity (e.g. efficiency), to the detriment of other important compressor characteristics. Moreover, multivariable objective function is used so that the optimum design of an aerospace or industrial compressor can be found using the same numerical procedure and ascribing suitable importance to the efficiency ($\eta_{TT}$), stall margin (identified by a coefficient $C_h$) and weight of the machine (identified by a specif area $A_{sp}$), whose linear combination represents an appropriate objective function.

For the design of an axial flow compressor stage, the following parameters are taken as the design variables:

Third International Conference on Inverse Design Concepts and Optimization in Engineering Sciences
(ICIDES-III), Editor: G.S. Dulikravich, Washington D.C., October 23-25, 1991.

$X_1$ = stage enthalpy drop ($\psi$)
$X_2$ = inlet flow coefficient ($\phi$)
$X_3$ = stator outlet absolute flow angle ($\alpha_3$)
$X_4$ = mean diameter of the stage ($D_m$)
$X_5$ = rotor axial velocity ratio ($AVR_R$)
$X_6$ = stator axial velocity ratio ($AVR_S$)
$X_7$ = stator solidity ($\sigma_S$)
$X_8$ = rotor solidity ($\sigma_R$)
$X_9$ = rotor blade chord to mean diameter ratio ($C_R/D_m$)
$X_{10}$ = stator blade chord to mean diameter ratio ($C_S/D_m$)
$X_{11}$ = stator max thickness to chord ratio ($(t_m/C)_S$)
$X_{12}$ = rotor max thickness to chord ratio ($(t_m/C)_R$)

The design process is shown in fig. 32. For given design specifications, the design parameters, defined at mean diameter, are guessed at the beginning of the computation and they define a first rough design wich is modified during the analysis design procedure in order to minimize the objective function. The evaluation of the efficiency is performed by using performance analysis of the stage defined by the actual values of the indipendent variables, while the stall margin is computed by using some simple correlation [19] suited for preliminary design studies.

The constraints of the optimization design method could be of two kinds. That is, rectangular constraints wich are directly applied on the design variables and they come from the field of the possible applicability of the correlations used in the objective function evaluation. However, a diret constraining of any single design variable does not ensure that, in a particular combination of them, some of the mechanical or fluid dynamic variables could exceed the usual limits. For these reasons, non-rectangular constraints have been chosen: they are related to the aerodynamic loading, flow instabilities, limiting flow rate through a flow path element, aeroelastic aspect of compressor blade rows, and noise generation. In order to take into account these non-rectangular constraints of the problem it is necessary to introduce in the optimization procedure the penalty function technique. The optimization problem is stated as a non linear programming problem as follows: find $X$ that minimizes

$$f(X) = G_\eta(1 - \eta_{TT}) + G_A(1 - A_{S_{sp}}) + G_C(1 - C_h) \qquad (1)$$

subject to the constraints

$$X_i^l < X_i < X^u \qquad i = 1, m \qquad g_j(X) \qquad j = 1, n \qquad (2)$$

where $G_\eta$, $G_A$ and $G_C$ are coefficients.Details of the method are given in Ref. [18].

In the following examples, the complete optimization method was first used with a single objective function coincident with $\eta_{TT}$ and then with a multivariable function ($\eta_{TT}$, $C_h$, $A_{sp}$).
From [17], the design of a stage of a small axial compressor (4 kg/s) with a high pressure ratio ($\beta_{TT} = 1.65$) is presented. The design variables are shown in Tab. 1, while Tab. 2 presents the numerical values of the constraints. The optimization has been performed with a single variable objective funcion, the total-to-total stage efficiency.
The initial stage efficiency value of 0.875 grows up to 0.927, with the absolute exit flow angle $\alpha_3 < 20^o$.
The optimized results shown in Tab 1 have been obtained by imposing different limits to the stage ($\alpha_3$). As shown, the design variables, $\phi$, $\psi$, AVR and $\sigma$ seem to be particularly sensitive to the $\alpha_3$ limits. The optimization procedure has carried out a reduction of the relative Mach number (to which shock losses are related) allowing for a remarkable reduction in the rotor losses ($\omega_{Ri} = 0.114$ and $\omega_{Ro} = 0.0675$).
Additional calculations have been performed by modifying the inlet flow algle ($\alpha_1$), simulating in this way the presence of an IGV or of a stage upstream. As an example, Tab. 3 shows the results obtained for $\alpha_1 = 0; 10; 20^o$.
In the previous examples it can be seen that, whereas $\eta_{TT}$ increases, the other significant design variables ($C_h$,$A_{sp}$) are drammatically reduced. This points out the necessety to operate with mixed objective function.

A design optimization has been performed using a multivariable objective function with different values of the coefficients $G_\eta$,$G_A$ and $G_C$, ranging from 0.0 to 1.0.
Table 4 shows the initial values of $\eta_{TT}$, $C_h$ and $A_{sp}$, and the final ones after the optimization process. From Tab. 4 it is evident that if $G_\eta = 0$, the values of $\eta_{TT}$ are absolutely unsatisfactory, especially in the case where $G_A$ and $G_C$ are unity. For this reason, the efficiency should always be present in the objective function. In the case where $G_\eta = 1$ and $G_C = 0$, a high reduction results in the stall margin (especially if $G_A = 1$).
If $G_\eta = G_A = G_C = 1$, the dominant effect of $G_A$ leads to a large increase in the specific area and also a corresponding decrease in the starting value of efficiency (from 0.87 to 0.78).
Finally, the analysis of the optimization with the multivariable objective function has been performed varying $G_A$ from 0 to 1, with $G_C$ as parameter and $G_\eta = 1$. The optimum efficiency, plotted in fig. 33, decreases greatly with $G_A$. The same trend, even if reduced in effects, is shown by $G_C$. Fig. 34 shows the stall margin coefficient; the influence of $G_A$ is negligible for high values of $G_C$, while if $G_C = 0$ the increase in $G_A$ is positive for the stall margin.

The one dimensional design procedure at mean diameter is simple and is justified by the need for an immediate definition of the global geometry of the machine and by the possibility of a preliminary design choice, but it does not provides any informations about the hub-to-tip geometry.
The one-D procedure has then been extended in [15],[18], by coupling the numerical optimization strategies with 2-D flow computation in the meridional plane (through-flow analysis) in order to have an optimized radial distribution of geometrical and aerodynamic quantities. This makes possible to optimize the radial distribution of the main geometrical and fluid dynamic parameters of the stage. Nevertheless, the method solves non linear equations by an iterative technique and therefore their introduction in the optimization procedure could be quite expensive as far as the computational time is considered due, also, to the high number of iterations required by the minimization.

Some difficulties is rappresented by the choice of the design variables. In a previous work [20], the authors chose to deal with three radial sections - root,mean and tip - for a total of ten design variables for each single row, considering fixed the geometry of the meridional section. The results obtained demonstrates the need for a better definition of the design variables and, therefore of the row geometry. In ref. [18], the coefficients of suitable polynomial that represents the 3-dimensional geometry of the row to be optimized were chosen as design variables.
The design variables -13 for each row- are all geometric, as opposed to the procedure presented in the preliminary design. This is due to the assumption that the optimization criteria will be applied to a machine of which the design is known, even if only in a preliminary way.
The evaluation of the objective function is obtained with a through-flow calculation by using a matrix method [21]. The code, furthermore, permits the calculation of the annulus wall boundary layer with an integral type solution [22] and the computation of the secondary deviation angle [23].

The general scheme is illustrated in fig. 35. Starting from initial data ($P_0$,$T_0$,$\beta_{TT}$,$m$) and from the mean diameter design variables ($X_i$), and working with a multivariable objective function, the mean diameter optimum geometry is obtained. From here, by considering a law of radial geometry distribution (e. g. the free vortex), the values of the the initial data of the through-flow calculation ($D_h$,$D_t$,$n$) and the new design variables (polynomial coefficients $a_i$) are obtained. Using the same algorithm of constrained minimization as in the previous case, the procedure continues until the objective is reached.
The optimization problem uses only one objective function coincident with the stage efficiency.

The procedure has been applied to solve two kinds of problems. In the first one the process is used to redesign an existing isolated transonic rotor. The one described in [24] is selected to verify the optimization process. The initial geometrical data of the rotor, which coincide with the polinomial functions to be optimized, are shown in figg. 36,37 and 38, respectively. The root chord is equal to 0.0388 m and is constant along the blade span. The calculation is carried out for the design conditions: $m = 96.18 kg/s$ and $n = 8870 rpm$. The initial efficiency (original geometry) is equal to 0.897, while the value obtained at the end of the optimization process is 0.943, greater than a 4 percent increase. Fig. 39 illustraes the objective function history during the optimization. In figg. 36, 37 and 38 in addition to the initial radial distributions, the optimized values are also given; it is possible to note how the angle $\beta_{1b}$ has undergone slight variation, with the maximum variation at the root ($4^o$). The angle $\beta_{2b}$ shows the maximum shift with respect to the initial value at meadspan of the blade ($6^o$). This involves an increase of the blade curvature in the central zone with slight reduction in the root and tip regions. The solidity is reduced along nearly all the span, while at tip it change from 1.30 to 1.41. The maximum thickness/chord ratio has, at the end of the optimization, a more uniform radial distribution. The optimization operates in the sense of a reduction of the diffusion factor in the $R < 0.4$ region (fig. 40), while in the upper zone $D_f$ increases. For $R < 0.6$, the loss reduction is significant as shown in fig. 41; in the tip region, where a great deal of the losses is due to the shock, although a reduction occurs (from 0.062 to 0.049), it appears to be more contained.

The second example is relative to the use of both procedures (pitchline and throughflow) in order to design a stage working from the following informations: mass flow rate= 4kg/s; pressure ratio $\beta_{TT} = 1.60$; $P_{01} = 101.3kPa$; $T_{01} = 300K$. The initial optimization procedure is carried out with an objective function having the following weights: $G_\eta = 1$, $G_C = 0.0$, $G_A = 0.0$, and with a higher constraint for $\alpha_3$ of $10^o$.
The meridional section optimized with such a procedure is illustrated in fig. 42. The rotational speed is 39,500 rpm; optimized efficiency is equal to 0.91, the stall margin is $C_h = 0.50$ and the specific inlet area is $A_{sp} = 170$.
The radial distribution of geometrical characteristics of the blade, from which the new design variables $a$ are obtained, was aquired by considering the free vortex law for the rotor and inlet section of the stator. For the stator outlet section, the angle $\alpha_{3b}$ was chosen in a different way (fig. 43). Optimization results are shown and compared with starting values in the above mentioned figures.
As far as efficiency is concerned, it must be pointed out that the value calculated with pitchline analysis differs from the initial finding obtained with the through-flow calculations. This latter, however, changes with the second optimization process from 0.844 to 0.905, showing at the same time a sufficiently rapid increase.

The previous examples have shown that the optimization technique allows a design of turbomachinery components with high degree of efficiency not only in one-dimensional approach, but also in an integrated analysis in the meridional plane where an optimal radial distribution is obtained for geometrical and aerodynamic quantities.
The same procedure has been applied by the authors to solve optimization problems for multistage axial flow turbines ([25]).

## 3 Inverse wing section design

From a fluid dynamic point of view the design of an airfoils looks for a geometry wich satisfy the equation of motion, given some boundary conditions. Two kinds of methodology can be used: the first one imposes some parameters (such as pressure, Mach number distribution, etc...) on the surfaces, while the second one prescribes some global properties to the flow field, such as minimum drag, shock-free, minimum entropy generation, etc... Both of them require some constraints in order to obtain a final airfoil shape with physical meaning.
As far as a design technique of the first type is conceived, and in the light of the well-posedness of the problem, the distribution of the flow parametes must satisfy some constraints in order to have the solution of the inverse problem for incompressible flow.
A methodology for solving inverse problem for airfoils by prescribing a pressure or velocity distribution is presented in ref. [26]. The inverse technique there presented is based on conformal mapping (ref. [27], [28]) for inviscid incompressible flow and it has been extended to the compressible subsonic flow case by applying the Karman-Tsien transformation. The assumption of inviscid flow is sufficiently approximated unless low Reynolds numbers are considered, when the boundary layer thickness can change significantly the resulting geometry. In this case the model is still valid, but the new surface is obtained by the displacement thickness given by the imposed pressure distribution.
The method outlined in ref. [26], consists in mapping the phisical domain $z(x, y)$, external to the closed line, in a seminfinity strip on the computational domain $\zeta(\xi, \eta)$ with $\eta > 0$ and $-\pi/4 \le \xi \le \pi/4$ (fig. 44).
The airfoils is approximated by rectilinear elements, and the mapping function, valid for poligonal contours

(ref. [26]), can be written in general form:

$$\frac{\partial z}{\partial \zeta} = f(M, \zeta, a_m, \alpha_m, g_m, C_m) \qquad m = 1, N \tag{3}$$

where M is a scale factor, $a_m$ represents the abscissa in the computaional domain of the nodal points of the elements, $g_m$ are function of $\zeta$ and the position of the $m_{th}$ element on the computational domain, and, finally, $C_m$ depend on the change of the tangent to the airfoil along the element $m_{th}$ as function of $a_m$. The $C_m$ values, which are known in a direct analysis because the geometry is given, in the inverse design they rapresent the unknowns of the problem.
In order to evaluate the $C_m$, the complex potential is imposed on the central point of the N-2 elements, where the modulus of the velocity is known. The resulting system with $C_m(m = 1, N + 1)$ unknowns is closed by giving the velocity and incidence at infinity, by imposing the Kutta condition, two geometrical constraints at the trailing edge in order to have a closed profile, and, finally, by imposing the tangent at leading edge to be perpendicular to the chord. Moreover, if the compressible flow is considered, the Karman-Tsien relationship is used to trasform the compressible distribution on a fictitious incompressible distributions.
Since the coefficient of system of equations are function of the position of nodal points in the computational domain which are unknown, an iterative procedure is followed:

1. An initial guessed distribution of nodal points is assumed in the computational domain
2. The system equation is solved by Gauss-Siedel method
3. The equation 3 is integrated by assuming a value of M; the airfoil is obtained in the phisycal plane and then M is scaled in order to have a computed chord equal to the prescribed one
4. If the position of the nodal points does not coincide with the previous values, the abscissa of these points are updated
5. The iterative process restarts from point 2 by using the new values of $C_m$

The method has been applied to the design of airfoils for wich the incompressible solution is known. Fig. 45 shows the incompressible velocity distribution associated to the symmetrical Karman-Treffez airfoil without incidence, wich is prescribed to solve inverse problem.
The resulting airfoil is shown in fig. 46. Here different solutions, obtained with 16 (triangles), 32 (circles) and 64 (plus) elements, are compared with the exact one. For the 64 elements, tab. 5 shows the abscissa of nodal points, the exact values $Y_E$ and the computed $Y_N$ coordinate, and the error with respect to the maximum thickness.
A further example relative to the Karman-Treffez airfoil with camber and $5^o$ incidence, with the prescibed velocity distribution given in fig. 47, is shown in fig. 48.
The method, which seems to be very accurate in the incompressible case, has been extended to the design problem by considering compressible subsonic flow. In this case also airfoils from catalogue have been selected as test cases. For the NACA0012 airfoils with $M_\infty = 0.72$, $\alpha_\infty = 0^o$; and $M_\infty = 0.5$, $\alpha_\infty = 3^o$, by prescribing the pressure coefficient reported in figs. 49 and 50, respectively, the results obtained by using 32 elements are shown in figs. 51,52.
Also for the compressible case the method seems to be very accurate, even when the Mach number is very close to one on the airfoils.

Third International Conference on Inverse Design Concepts and Optimization in Engineering Sciences
(ICIDES-III). Editor: G.S. Dulikravich, Washington D.C., October 23-25, 1991.

## References

[1] L. Zannetti, F. Larocca, *Inverse Methods for 3-D Internal Flows*, VKI Lecture Series 1990-8, Bruxelles, 14-18 May, 1990.

[2] L. Zannetti, *Time Dependent Method to Solve Inverse Problems for Internal Flows*, AIAA J., 18 July 1980, pp. 754-758.

[3] L. Zannetti, M. Pandolfi, *Inverse Design Techinque for Cascades.* NASA CR 3836, Nov. 1984.

[4] L. Zannetti, *A Natural Formulation for the Solution of 2D or Axisymmetric Inverse Problems*, Int. J. Num. Meth. in Eng., Vol. 22, Feb. 1986, pp. 451-463.

[5] L. Zannetti, T. T. Ayele, *Time Dependent computation of the Euler Equations for Designing Fully 3D Turbomachinary Blade Rows, Including the Case of Transonic Shock Free Design*, AIAA 25th Aerospace Sciences Meeting, Reno, Nevada, Jan. 1987, AIAA-87-0007.

[6] L. Zannetti, F. Larocca, *Time Dependent Solution of Multidimensional Inverse Problems*, 2nd Int. Conf. on Inverse Design Concept Optimization in Engineering Sciences, University Park, Pen. Oct. 1988.

[7] G. Meauze, *An Inverse Time Marching Method for the Definition of Cascade Geometry*, ASME Paper 81-GT-167.

[8] F. Ringleb, *Exacte Losungen der Differentialk-gleichungen einer adiabatischen Gasstromung*, ZAMM, Vol. 20, N. 4, 1940, pp. 785-798.

[9] G. Moretti, *The lambda-scheme*, Comput. Fluids, 7, 191-205 (1979).

[10] G. Moretti, L. Zannetti, *A New, Improved Computational Technique for Two-dimensional Unsteady Flow*, AIAA J., 22 June, 1984, pp 758-765

[11] L. Zannetti, B. Favini, *About the numerical modelling of multidimensional unsteady compressible flow*,Comput. Fluids, 17 289-299 (1989).

[12] L. Zannetti, B. Favini, *A difference scheme for weak solution of gasdynamic equations*, AIAA Paper 87-0537.

[13] G. Moretti, M. Pandolfi, *Critical study of calculations of subsonic flow in ducts*, AIAA Jou., 19 April 1981, pp. 449-457.

[14] M. Pandolfi, L. Zannetti, *Some permeable boundaries in multidimensional flows*, 6th Int. Conf. on Num. Meth. in Fluid Dyn., Tbilisi 1978, Lecture Notes in Physics N. 90, Springer-Verlag, pp. 439-446.

[15] A. Massardo, A. Satta, *Procedura di ottimizzazione per il Progetto dei Compressori Assiali*, VIII AIMETA 1986, Torino, Italy, 29 Sept-3 Oct, 1986.

[16] A. Massardo, C. Serrati, *Codice di Ottimizzazione del Progetto di Turbomacchine Assiali*, DINE-SMF, Genova, Italy, Jan 1985.

[17] A. Massardo, A. Satta, *Axial Flow Compressor Design Optimization: Part I - Pitchline Analysis and Multivariable Objective Funcion Influence*, ASME J. of Turbomachinery, Vol. 112, July 1990, pp 399-404.

[18] A. Massardo, A. Satta, M. Marini, *Axial Flow Compressor Design Optimization: Part II - Throughflow Analysis*, ASME J. of Turbomachinery, Vol. 112, July 1990, pp 405-410.

[19] C. C. Kock, *Stalling Pressure Rise Capability of Axial Flow Compressor Stages*, ASME J. Engineering for Power, Vol. 103, 1981, pp 645-656.

[20] A. Massardo, A. Satta, *The Use of Optimization Technique and Through-flow Analysis for the Design of Axial Compressor Stages*, Proceedings 8th Turbomachinery Conference, Budapest, Hungary, 1987.

[21] D. Breschi, A. Massardo, *Metodo Matriciale per il Calcolo Meridiano di un compressore assiale pluristadio*, 37th ATI Confernce, Padova, Italy, 1982.

[22] H. Perkins, J. Horlock, *Annulus Wall Boundary Layer in Turbomachines*, AGARDOGRAPH.

[23] A. Massardo, A. Satta, *A Correlation for the Secondary Deviation Angle*, ASME paper No. 85-GT-36.

[24] D. R. Seyler, J. P. Gostelow, *Single Stage Experimental Evaluation of High Mach Number Compressor Rotor Blading, Part 2. Performance of Rotor 1-B*, NASA CR-582.

[25] A. Massardo, A. Satta, *Industrial Design Optimization of Small and Large Size Axial Turbines*, ASME paper No. 90-GT-220.

[26] B. Fortunato, A. Lippolis, *Progetto di Profili Aerodinamici Mediante Trasformazione Conforme*, Atti dell' Ist. di Macchine ed Energetica dell' Universita' di Bari, Italy, Sept, 1990.

[27] A. Lippolis, *A Grid Generation Technique Based on a Conformal transformation*, Atti dell' Ist. di Macchine ed Energetica dell' Universita' di Bari, Italy, Oct, 1990.

[28] L. C. Woods, *The Theory of Subsonic Plane Flow*, Cambridge, University Press, 1961.

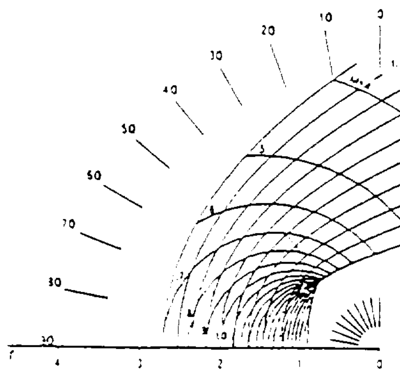

Figure 1: Ringleb flow

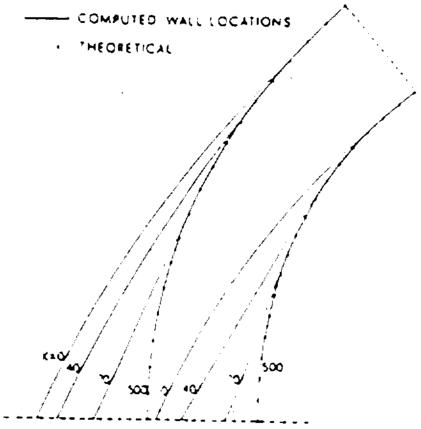

Figure 2: time evolution of the movable walls

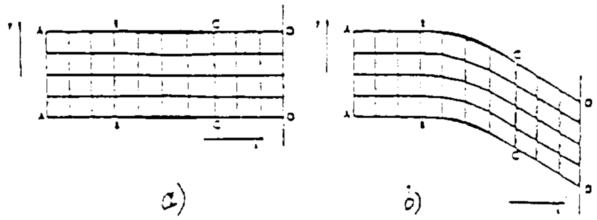

a) b)

Figure 3:

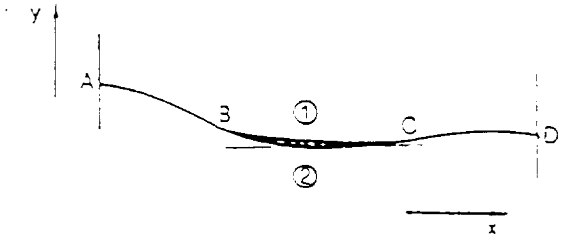

Figure 4:

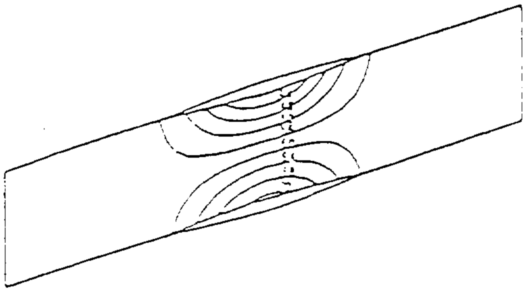

Figure 6:

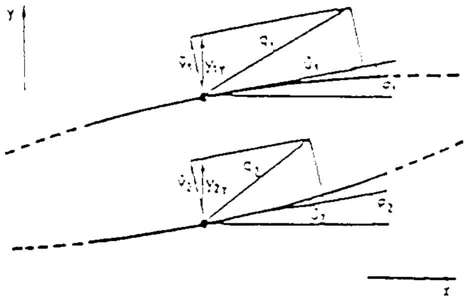

Figure 5:

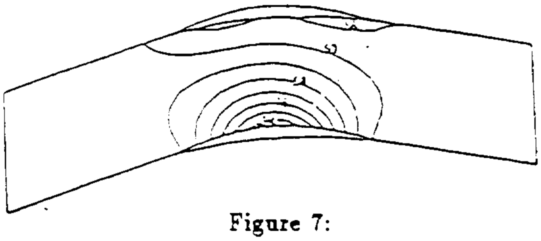

Figure 7:

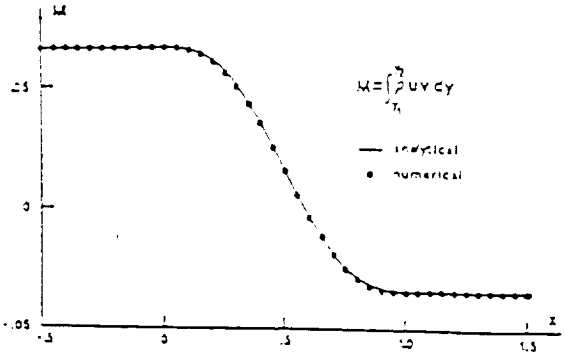

Figure 8:

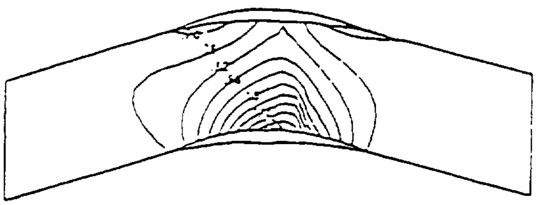

Figure 9:

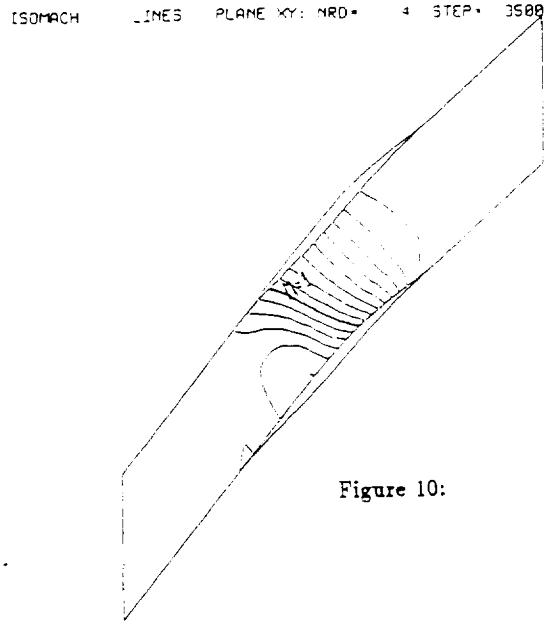

Figure 10:

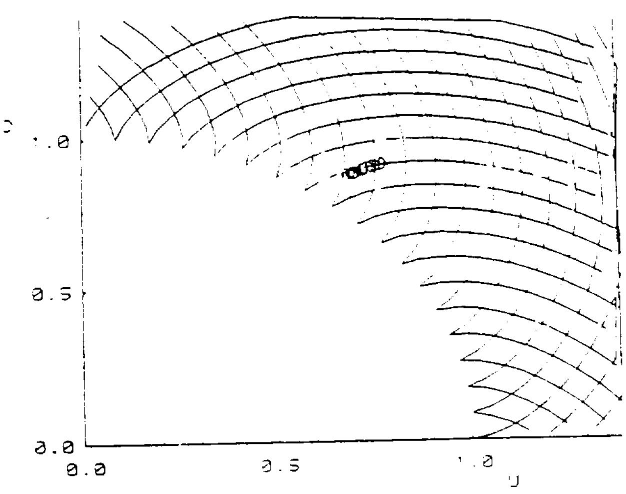

Figure 11:

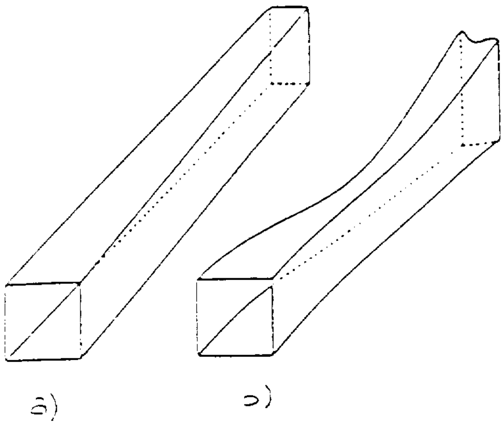

Figure 12:

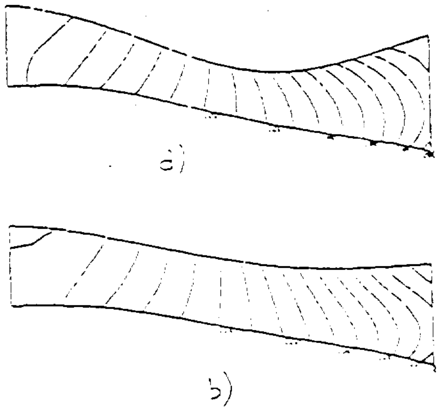

Figure 13:

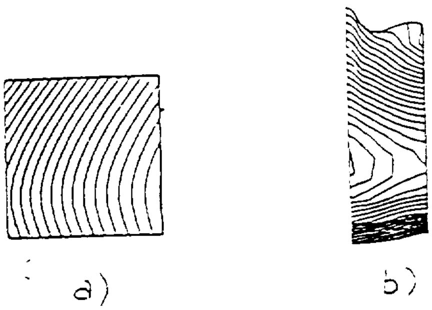

Figure 15:

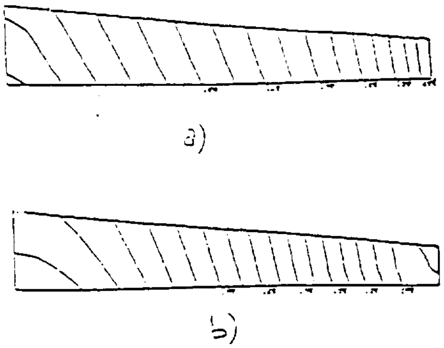

Figure 14:

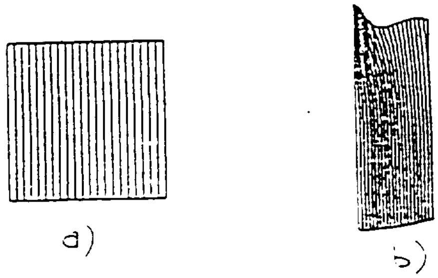

Figure 16:

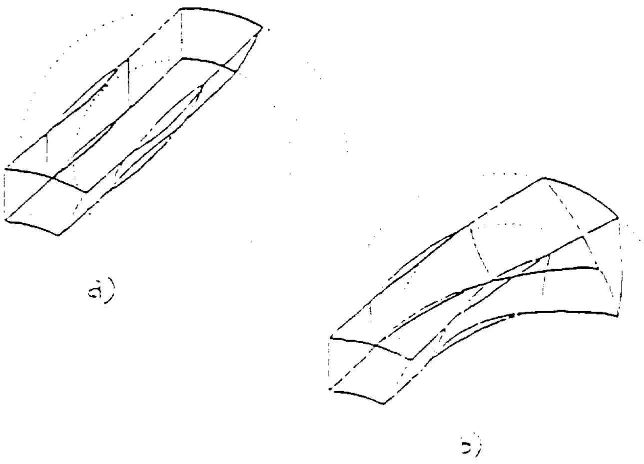
a)

b)

Figure 17:

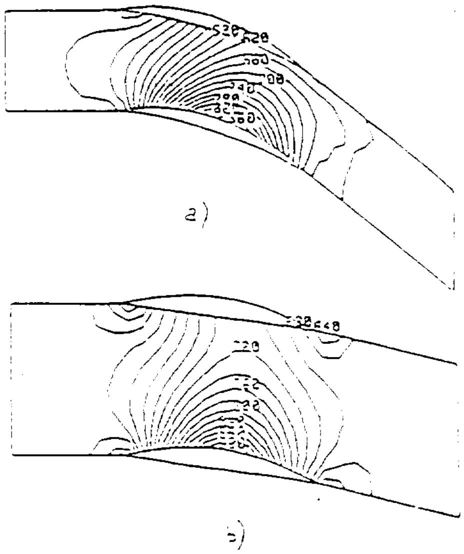

Figure 18:

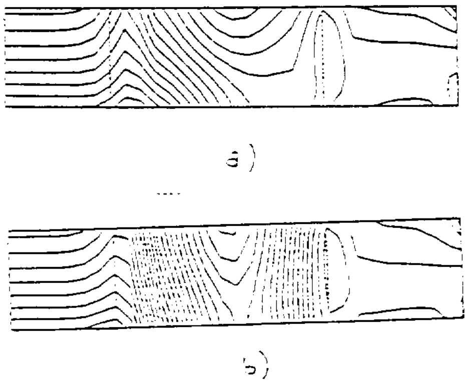
a)

b)

Figure 19:

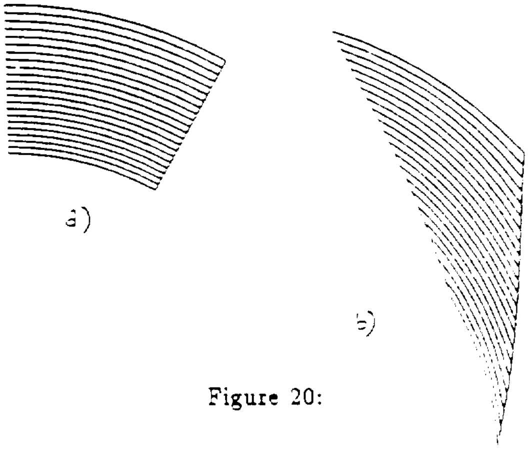
a)

b)

Figure 20:

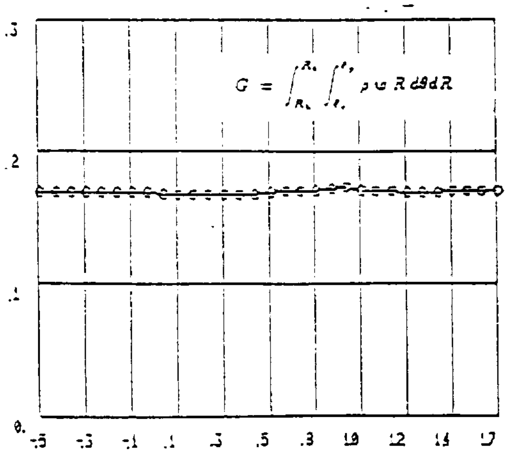

Figure 21:

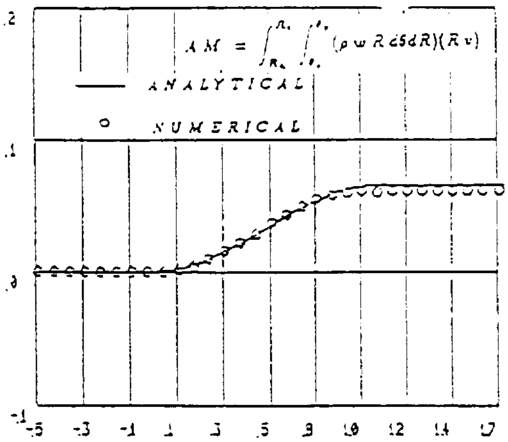

Figure 22:

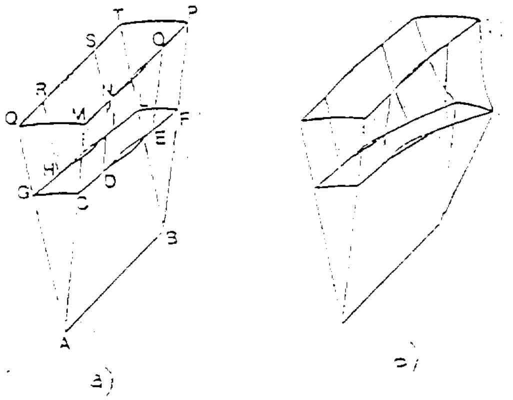

Figure 23:

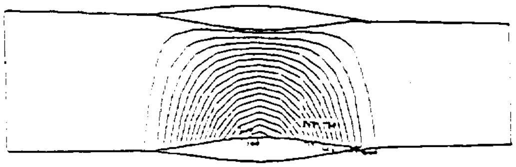

Figure 24:

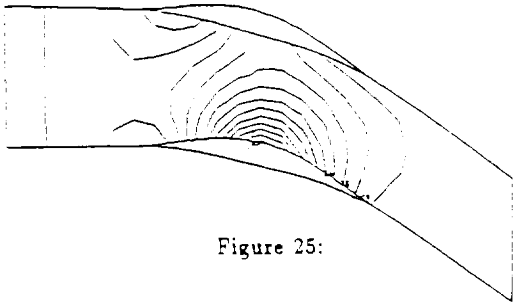

Figure 25:

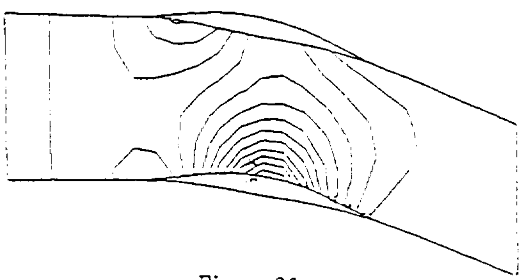

Figure 26:

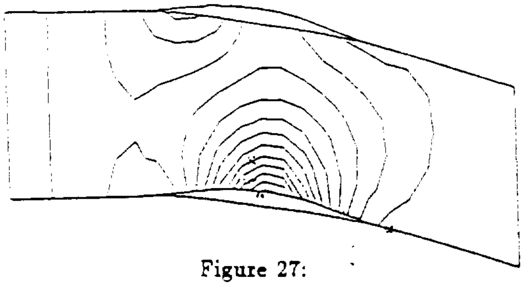

Figure 27:

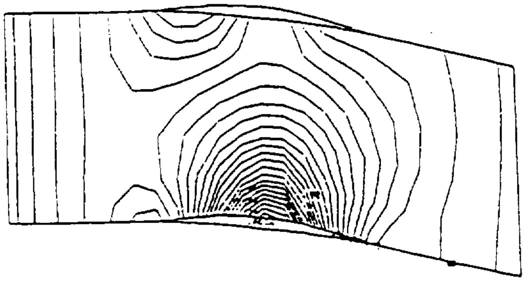

Figure 28:

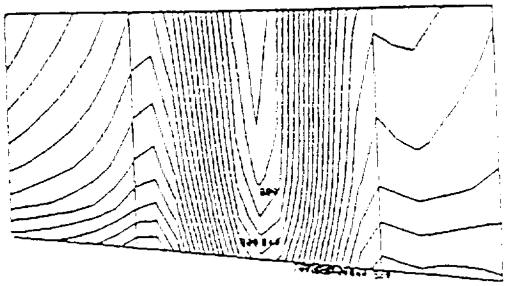

Figure 29:

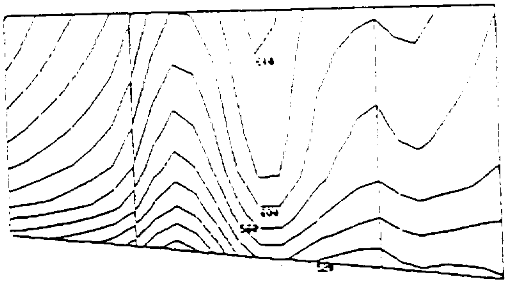

Figure 30:

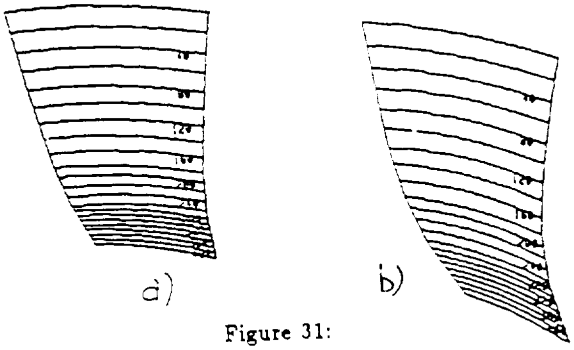

Figure 31:

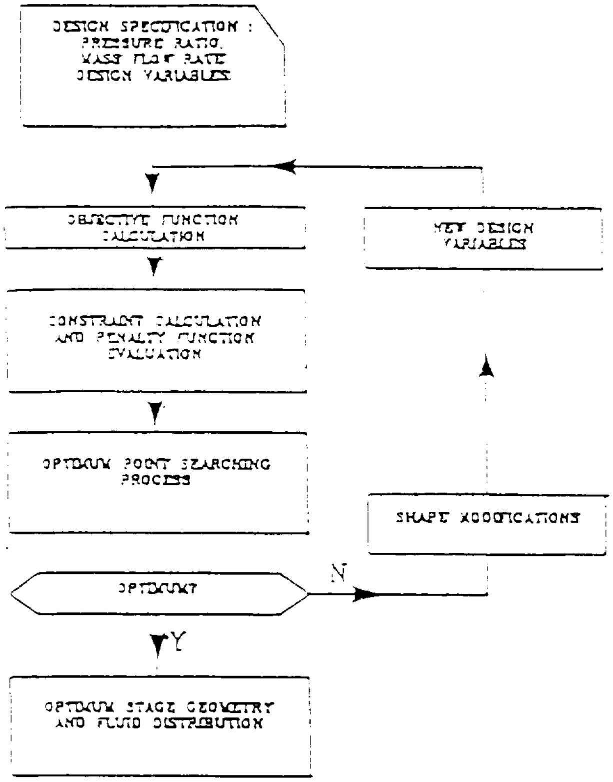

Figure 32: General optimisation flow chart

| — | $\alpha_1 = 0°$ | | $\alpha_1 = 10°$ | | $\alpha_1 = 20°$ | |
|---|---|---|---|---|---|---|
| — | i | o | i | o | i | o |
| $\eta_{TT}$ | 0.870 | 0.914 | 0.884 | 0.914 | 0.883 | 0.910 |
| $A_{so}$ | 180 | 166 | 178 | 178 | 176 | 177 |
| $C_m$ | 0.541 | 0.516 | 0.534 | 0.512 | 0.526 | 0.531 |
| $\omega_R$ | 0.128 | 0.082 | 0.103 | 0.076 | 0.088 | 0.075 |
| $\omega_S$ | 0.061 | 0.047 | 0.069 | 0.051 | 0.089 | 0.063 |
| $M_{r1m}$ | 1.224 | 1.081 | 1.134 | 1.089 | 1.052 | 1.049 |
| $M_{a3}$ | 0.569 | 0.546 | 0.564 | 0.705 | 0.826 | 0.780 |

Table 3 Influence of $\alpha_1$ value on the optimization ($OBJ = 1 - \eta_{TT}$; $\alpha_3 = 20$ deg; DCA blade; $\beta_{TT} = 1.75$; $i$ = initial; $o$ = optimum)

| $G_\eta$ | $G_A$ | $G_C$ | $\eta_{TT}$ | $A_{so}$ | $C_m$ |
|---|---|---|---|---|---|
| - | - | - | 0.875 | 171.38 | 0.535 |
| 1 | 0 | 0 | 0.921 | 158.88 | 0.481 |
| 0 | 1 | 0 | 0.600 | 225.74 | 0.539 |
| 0 | 0 | 1 | 0.415 | 145.72 | 0.598 |
| 1 | 1 | 1 | 0.786 | 208.95 | 0.572 |
| 1 | 0 | 1 | 0.888 | 162.04 | 0.553 |
| 1 | 1 | 0 | 0.854 | 208.60 | 0.478 |
| 0 | 1 | 1 | 0.730 | 213.90 | 0.572 |
| 1 | 0.5 | 1 | 0.891 | 187.63 | 0.577 |

Table 4 Influence of the different coefficient values in the multivariable objective function (C – series; $\dot{m} = 4$ kg/s; $\alpha_3 \leq 20$ deg; $\beta_{TT} = 1.65$)

| DESIGN VARIABLES | STARTING VALUE | OPTIMUM VALUE | | |
|---|---|---|---|---|
| | | $\alpha_3 \leq 20°$ | $\alpha_3 \leq 10°$ | $\alpha_3 \leq 0°$ |
| $\psi$ | 0.4 | 0.496 | 0.462 | 0.438 |
| $\phi$ | 0.45 | 0.465 | 0.471 | 0.464 |
| $\alpha_3$(°) | 0.0 (0.0) | 19.39 | 9.19 | 0.0 |
| $D_m$(m) | 0.170 | 0.163 | 0.159 | 0.158 |
| $AVR_R$ | 1.15 | 1.04 | 1.00 | 1.00 |
| $AVR_S$ | 1.20 | 1.32 | 1.40 | 1.48 |
| $\sigma_S$ | 1.3 | 1.50 | 1.50 | 1.74 |
| $\sigma_R$ | 1.5 | 1.25 | 1.25 | 1.27 |
| $C_R/D_m$ | 0.200 | 0.200 | 0.200 | 0.222 |
| $C_S/D_m$ | 0.140 | 0.128 | 0.13 | 0.122 |
| $t_m/C_R$ | 0.050 | 0.0518 | 0.0487 | 0.0447 |
| $t_m/C_S$ | 0.050 | 0.0498 | 0.0502 | 0.0745 |
| $OBJ=(1-\eta_{TT})$ | 0.875 | 0.927 | 0.920 | 0.917 |

$\dot{m} = 4$ kg/s ; $\beta_{TT} = 1.65$ , $P_{01} = 101300$ Pa ,
$T_{01} = 300$ K ; $\alpha_1 = 0°$.

Table 1 Optimization results for three different limits imposed a $X_3 = \alpha_3$

| | | |
|---|---|---|
| $0.03 < H_1/D_m < 0.3$ | $0.03 < H_2/D_m < 0.3$ | $0.03 < H_3/D_m < 0.3$ |
| $50 < U < 450$ (m/s) | $0.5 < (H_1/C_R) < 4$ | $0.5 < (H_2/C_S) < 3$ |
| $0.1 < M_{a1} < 0.7$ | $0.1 < M_{a2} < 0.9$ | $0.1 < M_{a3} < 0.9$ |
| $0.1$ (mm) $< \tau < 1$ (mm) | $0.001 < \tau/H_1 < 0.01$ | $\sigma_{stress} < \sigma$ [illegible] |
| $15 < Z_R < 50$ | $20 < Z_S < 100$ | 1 [illegible] $< 2.0$ |
| $0.35 < C_{mR}$ | $0.35 < C_{mS}$ | $140 < A_{so}$ |
| $0.75 < \eta_{TT}$ | $1 < H_1/H_2 < 2.5$ | $1 < H_2/H_3 < 1.5$ |
| $0.2 < \phi < 0.60$ | $0.15 < \psi < 0.5$ | $0° < \alpha_3 < 20°$ |
| $0.15$ m $< D_m < 0.3$ m | $0.8 < AVRR < 1.5$ | $1.0 < AVRS < 1.5$ |
| $1.0 < \sigma_S < 2.0$ | $0.5 < \sigma_R < 2.0$ | $0.2 < (C_R/D_m) < 0.5$ |
| $0.1 < (C_S/D_m) < 0.5$ | $0.005 < (t_m/C)_R \leq 0.2$ | $0.005 < (t_m/C)_S < 0.2$ |

Table 2 Design constraints

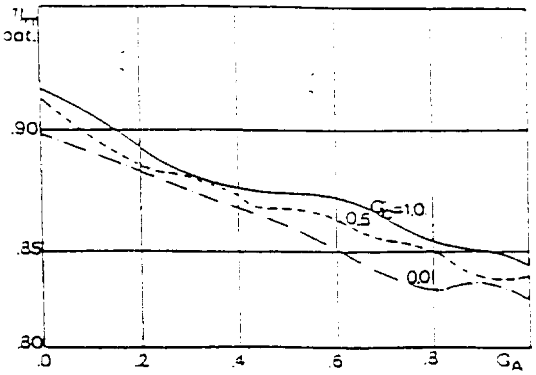

Figure 33: Efficiency diagram versus $G_A$ and $G_C$

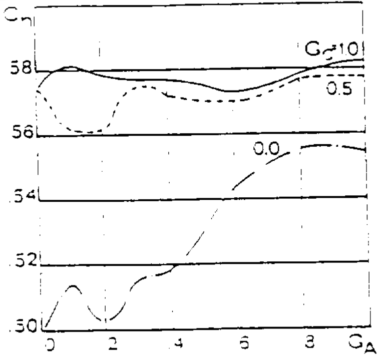

Figure 34: Influence of $G_A$ and $G_C$ on stall margin

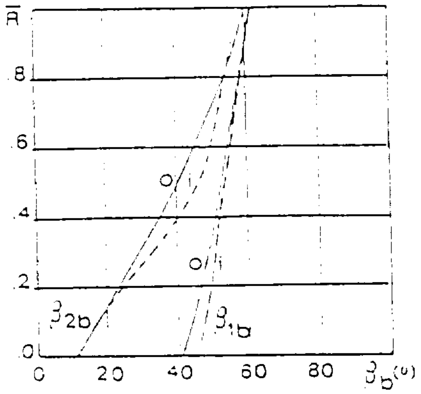

Figure 36: Radial distribution of blade anlgles angles
(i=initial; o=optimum)

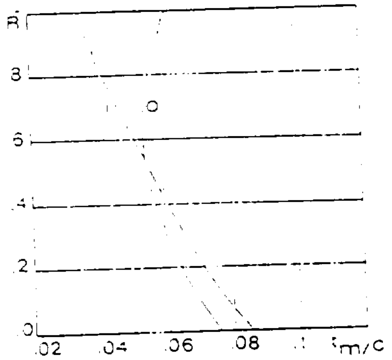

Figure 37: Radial distribution of max blade thickness

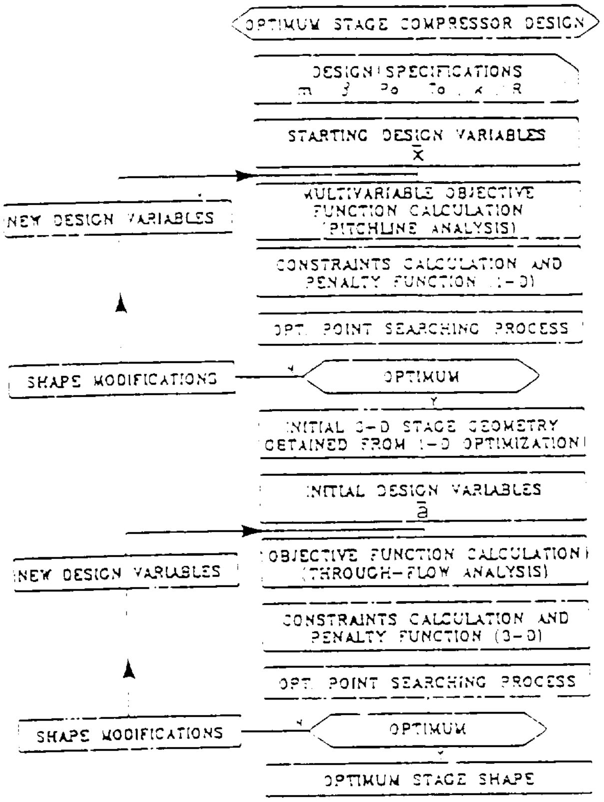

Figure 35: Optimum complete stage design

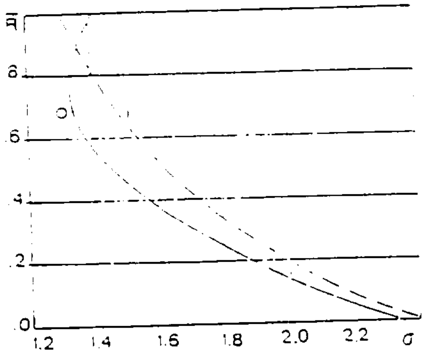

Figure 38: Radial distribution of solidity

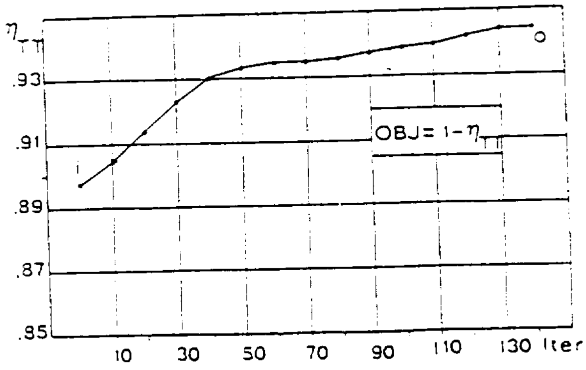

Figure 39: Optimization history of rotor total-to-total efficiency

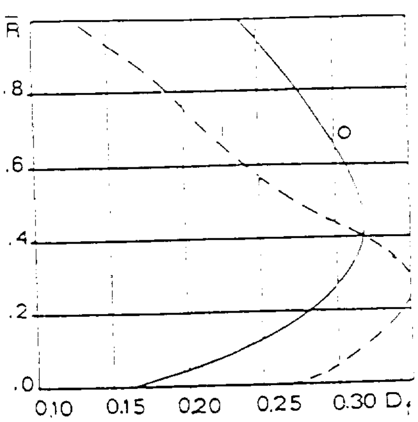

Figure 40: Radial distribution of diffusion factor

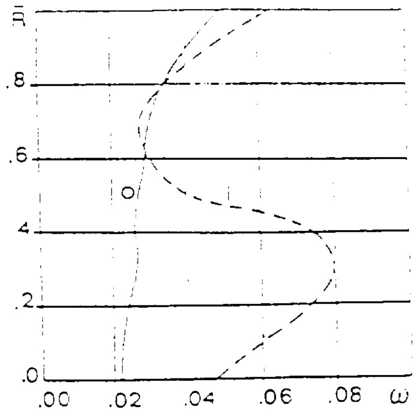

Figure 41: Radial distribution of total pressure loss

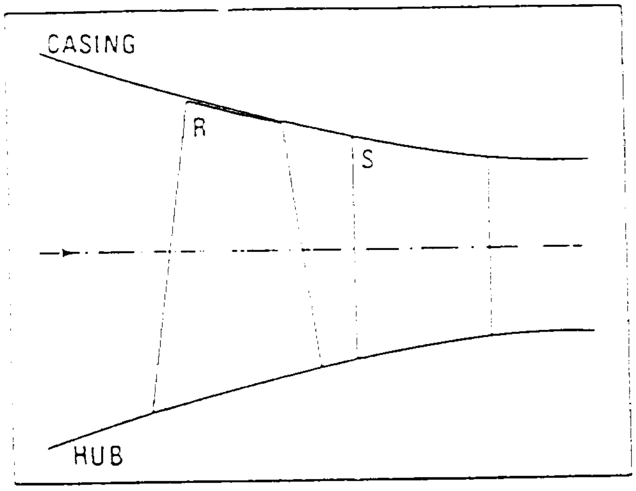

Figure 42: Meridional section

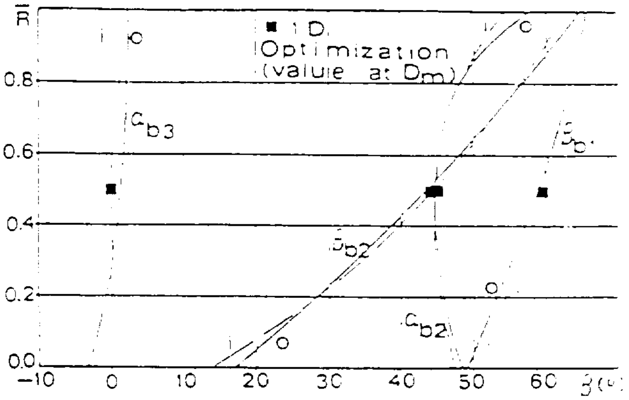

Figure 43: Stator and rotor angles

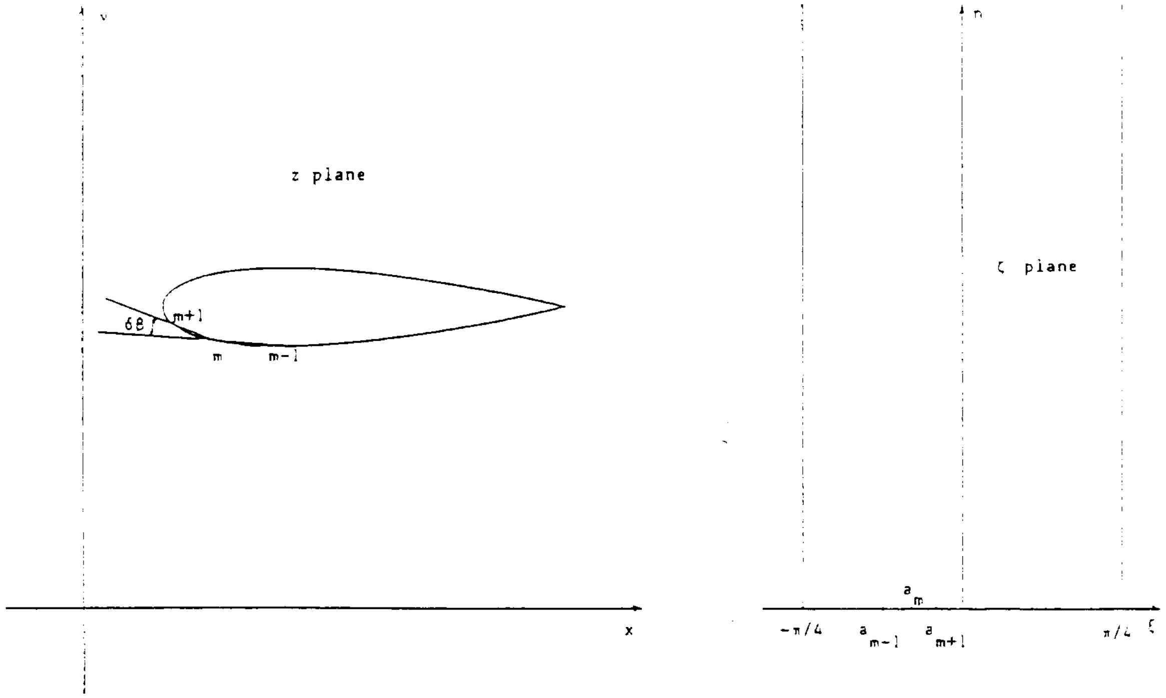

Figure 44: Physical and computational domain

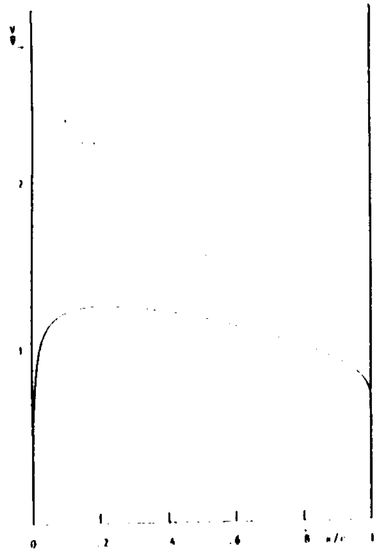

Figure 45: Karman-Treffez airfoil: velocity distribution

Tab 5 KARMAN-TREFFTZ α =0°

| X | $Y_E$ | $Y_N$ | εZ |
|---|---|---|---|
| .00000 | .000000 | 000000 | .00 |
| .00241 | .011094 | .011737 | .34 |
| .00961 | .022164 | 022873 | .37 |
| .02153 | .033113 | .033607 | .26 |
| .03806 | .043774 | 044191 | .22 |
| .05904 | .053944 | .054310 | .19 |
| .08427 | .063411 | .063740 | .17 |
| .11349 | .071966 | 072266 | .16 |
| .14645 | .079420 | .079695 | .14 |
| .18280 | .085607 | 085861 | .13 |
| .22221 | .090393 | .090628 | .12 |
| .26430 | .093683 | .093900 | .11 |
| .30866 | .095420 | .095621 | .11 |
| .35486 | .095593 | .095779 | .10 |
| .40245 | .094232 | .094403 | .09 |
| .45099 | .091412 | .091571 | .08 |
| .50000 | .087252 | .087397 | .08 |
| .54901 | .081906 | .082039 | .07 |
| .59754 | .075562 | .075683 | .06 |
| .64514 | .068437 | 068546 | .06 |
| .69134 | .060764 | .060862 | .05 |
| .73570 | .052789 | .052876 | .05 |
| .77778 | .044759 | .044835 | .04 |
| .81720 | .036911 | .036977 | .03 |
| .85355 | .029468 | .029523 | .03 |
| .88650 | .022624 | 022669 | .02 |
| .91573 | .016542 | .016577 | .02 |
| .94096 | .011345 | .011372 | .01 |
| .96194 | .007117 | .007134 | .01 |
| .97847 | .003894 | .003903 | .00 |
| .99039 | .001671 | .001672 | .00 |
| .99759 | .000400 | .000397 | .00 |
| 1.00000 | .000000 | 000000 | 00 |

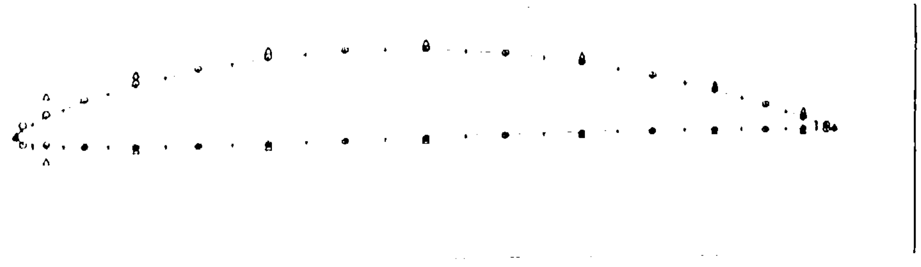

Figure 48: Karman-Treffez airfoil with camber and 5° incidence

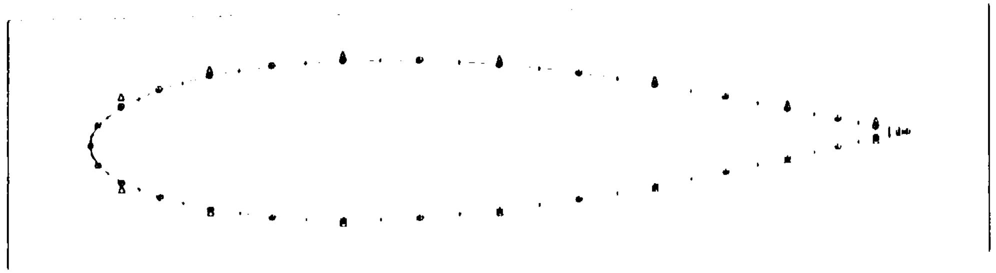

Figure 46: Karman-Treffez airfoil: exact and numerical solution α:0

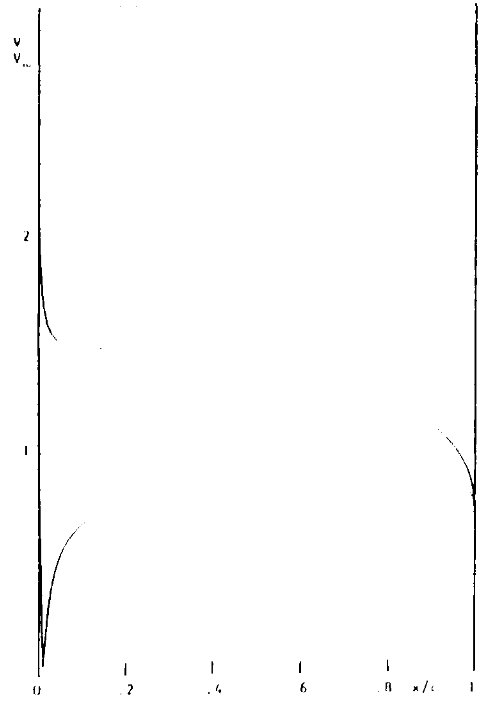

Figure 47: Karman Treffez airfoil: velocity distribution

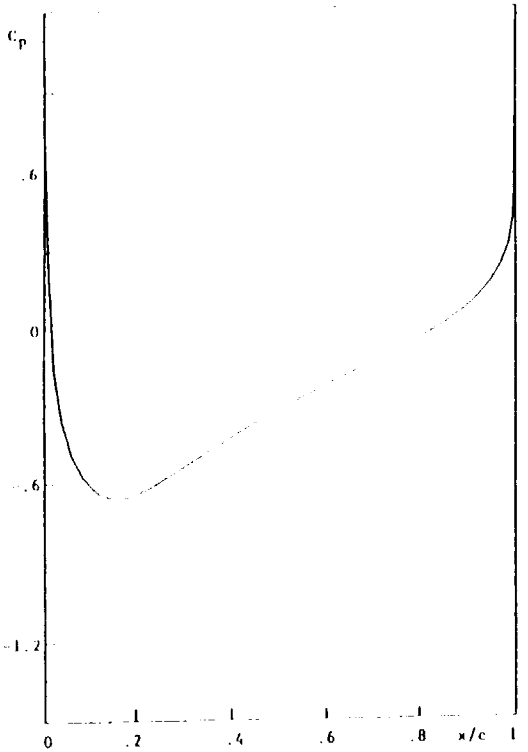

Figure 49: NACA0012 $M_\infty = 0.72$, $\alpha_\infty = 0°$

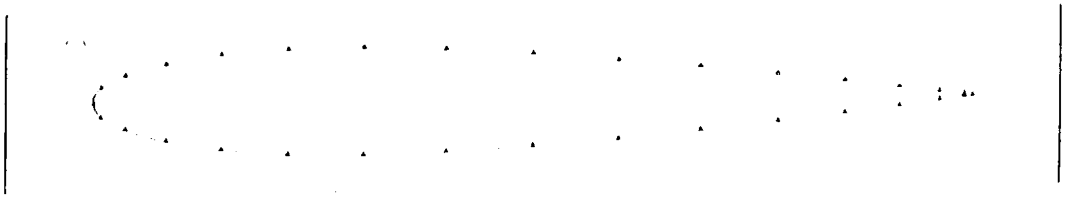

Figure 50: NACA0012 $M_\infty = 0.5$, $\alpha_\infty = 3°$: exact and computed solutions

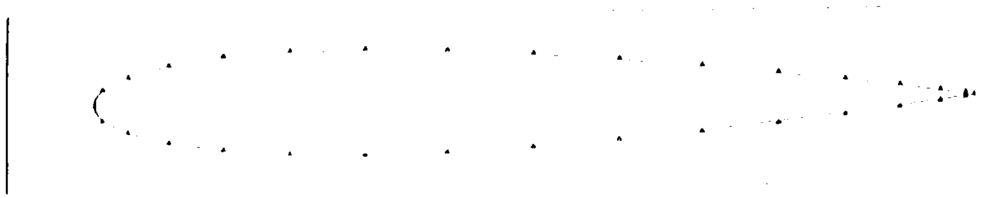

Figure 52: NACA0012 $M_\infty = 0.5$, $\alpha_\infty = 3°$: exact and computed solutions

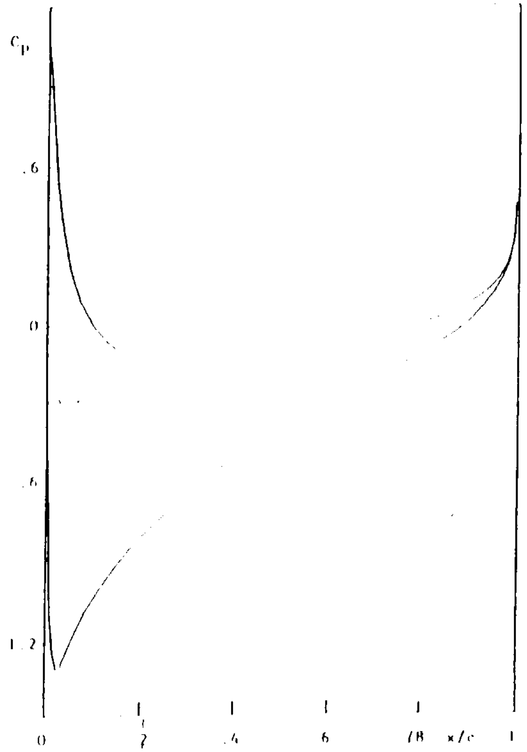

Figure 51: NACA0012 $M_\infty = 0.5$, $\alpha_\infty = 3°$